

Addressing Data Scarcity in 3D Trauma Detection through Self-Supervised and Semi-Supervised Learning with Vertex Relative Position Encoding

Shivam Chaudhary
Pattern Recognition Lab
FAU Erlangen-Nürnberg
shivam.chaudhary@fau.de

Sheethal Bhat
Pattern Recognition Lab
FAU Erlangen-Nürnberg
sheethal.bhat@fau.de

Andreas Maier
Pattern Recognition Lab
FAU Erlangen-Nürnberg
andreas.maier@fau.de

Abstract—Accurate detection and localization of traumatic injuries in abdominal CT scans remains a critical challenge in emergency radiology, primarily due to severe scarcity of annotated medical data. This paper presents a label-efficient approach combining self-supervised pre-training with semi-supervised detection for 3D medical image analysis. We employ patch-based Masked Image Modeling (MIM) to pre-train a 3D U-Net encoder on 1,206 CT volumes without annotations, learning robust anatomical representations. The pre-trained encoder enables two downstream clinical tasks: 3D injury detection using VDETR with Vertex Relative Position Encoding, and multi-label injury classification. For detection, semi-supervised learning with 2,000 unlabeled volumes and consistency regularization achieves 56.57% validation mAP@0.50 and 45.30% test mAP@0.50 with only 144 labeled training samples, representing a 115% improvement over supervised-only training. For classification, expanding to 2,244 labeled samples yields 94.07% test accuracy across seven injury categories using only a frozen encoder, demonstrating immediately transferable self-supervised features. Our results validate that self-supervised pre-training combined with semi-supervised learning effectively addresses label scarcity in medical imaging, enabling robust 3D object detection with limited annotations. The code is available at <https://github.com/shivasmic/3d-trauma-detection-ssl>.

Index Terms—3D Object Detection, Self-supervised learning, Semi-Supervised Learning, Transformer, DETR, Relative Position Encoding, U-Net, Computed Tomography

I. INTRODUCTION

A. Background and motivation

Medical imaging plays a pivotal role in modern diagnostic workflows, with Computer Tomography (CT) scans being particularly valuable for detecting internal injuries and anatomical abnormalities. However, manual analysis of 3D medical volumes is time-intensive, requires expert knowledge, and is prone to inter-observer variability. The development of automated 3D object detection systems for medical imaging promises to improve diagnostic accuracy, reduce radiologist workload, and enable faster clinical decision-making, particularly in emergency settings where timely diagnosis is critical.

Traditional approaches to medical image analysis have predominantly relied on 2D slice-by-slice evaluation or 3D convolutions, which fail to capture complex spatial relationships inherent in volumetric data. Furthermore, the scarcity

of annotated medical datasets, where obtaining pixel-level segmentation masks requires significant expert time, poses a fundamental bottleneck for supervised learning approaches. In the RSNA abdominal trauma detection dataset used in this work, only 206 of 4711 available series contain segmentation masks, representing less than 5% labeled data. This severe label scarcity requires novel approaches that effectively leverage unlabeled data.

The development of robust 3D detection systems for medical imaging faces fundamental challenges stemming from the unique characteristics of medical data. Medical datasets typically contain severely limited labeled samples due to expensive and time-consuming expert annotation requirements, with our RSNA dataset containing only 206 labeled series among 4,711 total scans (4.4% labeled). This extreme scarcity makes traditional fully-supervised approaches impractical, while the computational demands of processing full 3D volumes (512×336×336 voxels) with direct 3D convolutions strain available hardware resources. Additionally, anatomical structures exhibit significant variability in shape, size, and location across patients due to individual demographics, pathology, and imaging protocols—unlike the relatively rigid objects common in natural image datasets.

Beyond data and computational constraints, 3D medical detection requires sophisticated spatial reasoning capabilities that conventional approaches fail to provide. Traditional 2D detection methods relying on center-point predictions inadequately capture the volumetric nature of irregularly-shaped organs and injuries, where single distance metrics cannot represent complex geometric relationships. Furthermore, generic 3D feature extractors pre-trained on natural videos or synthetic data transfer poorly to medical imaging, which exhibits distinct characteristics including limited color information, specific intensity distributions (Hounsfield Units), and highly domain-specific anatomical patterns that require specialized representation learning.

B. Proposed Approach

This research addresses label scarcity in 3D medical object detection through a two-stage learning framework. First,

we employ self-supervised Masked Image Modeling (MIM) to pre-train a 3D U-Net encoder on 1,206 unlabeled CT volumes, learning robust anatomical representations without annotations. Second, we leverage these pre-trained features for two downstream tasks: 3D injury detection using VDETR with Vertex Relative Position Encoding and semi-supervised consistency regularization on 2,000 additional unlabeled volumes, and multi-label injury classification with minimal fine-tuning. This approach enables effective learning from severely limited labeled data (144 volumes for detection, 2,244 for classification) while maintaining strong generalization to held-out test sets.

C. Paper Organization

The remainder of this paper is organized as follows: Section II reviews related work in 3D object detection, self-supervised learning, and medical image analysis. Section III details our data preprocessing pipeline and standardization procedures. Section IV describes the 3D U-Net encoder architecture and self-supervised pre-training methodology. Section V presents the VDETR decoder design with 3D Relative Positional Encoding. Section VI explains our two-phase training strategy. Section VII presents experimental results and evaluation metrics. Section VIII discusses limitations and future directions. Finally, Section IX concludes the paper.

II. LITERATURE OVERVIEW

The field of 3D object detection has evolved significantly from early approaches that relied heavily upon 2D slice-by-slice analysis or sliding window techniques, which fundamentally fail to capture the volumetric nature of 3D medical data. Traditional 3D object detection methods adapted natural image object detectors, such as Faster R-CNN [1], to volumetric data by replacing 2D convolutions with their 3D counterparts. However, these anchor-based approaches came with a price of extensive hyperparameter tuning and struggled with irregular anatomical shapes, which made them unfit for processing medical image data, since medical data is full of complex and irregular anatomical object shapes. VoteNet [2] came up with a voting mechanism to shift surface points toward object centers for grouping, enabling end-to-end learning from point clouds. More recent methods like FCAF3D [3] employ expansion-based approaches to generate virtual center features from surface features, thereby improving overall region proposal quality. However, all these fully convolutional approaches critically rely on large amounts of pixel-level annotations, which are prohibitively expensive in medical imaging, where only 4.4% of our dataset contains segmentation masks.

The introduction of DETR [4] revolutionized object detection by formulating it as a direct set prediction problem. It replaced the hand-designed components like non-maximum suppression and anchor generation through learnable object queries that attend to image features via cross-attention mechanisms, which enables end-to-end differentiable detection with elegant simplicity. Early 3D adaptations like 3DETR [5] and GroupFree [6] adapted the DETR framework to 3D point

clouds but achieved suboptimal results, particularly in medical imaging, due to their inability to learn accurate inductive biases from limited training data. Specifically, queries often attended to points far from target objects, violating the locality principle essential for effective detection. V-DETR [7] fundamentally addressed this limitation by introducing 3D Vertex Relative Position Encoding (3DV-RPE), which computes position encoding for each point based on its relative position to all eight vertices of predicted 3D boxes rather than just box centers, providing clear geometric information about whether points lie inside, outside, or on boundaries of objects. This corner-based encoding enables the model to learn locality even from limited data, achieving state-of-the-art results on indoor 3D detection benchmarks like ScanNetV2.

The scarcity of labeled medical data has driven substantial research in self-supervised learning (SSL) approaches capable of leveraging large volumes of unlabeled data to learn robust feature representations. Masked Image Modeling (MIM), inspired by masked language modeling in NLP, has emerged as an effective paradigm for visual representation learning. Masked Autoencoders (MAE) [8] demonstrated that masking random patches and reconstructing them provides robust supervision to models, enabling them to learn transferable features in natural images and achieving strong performance on downstream tasks with minimal fine-tuning. For medical imaging specifically, the importance of pre-training has been systematically investigated by Eckstein et al. [9], who demonstrated that self-supervised pre-training significantly improves 3D medical object detection performance, particularly when there is a scarcity of labeled data. Their work showed that pre-training on large-scale unlabeled medical volumes enables models to learn anatomical priors that substantially enhance detection accuracy compared to training from scratch.

Complementary to self-supervised pre-training, semi-supervised learning addresses label scarcity by enabling models to learn from abundant unlabeled samples while being guided by limited annotations during training. Mean Teacher [10] introduced the teacher-student framework where an exponential moving average (EMA) model serves as the teacher, providing pseudo-labels for unlabeled data that guide student model training through consistency regularization. This approach enforces prediction consistency between teacher and student models on perturbed versions of the same input, proving highly effective across various domains. For object detection specifically, Unbiased Teacher [11] adapted the teacher-student framework by addressing the confirmation bias problem where incorrect teacher predictions reinforce student errors, introducing focal loss weighting to handle class imbalance in pseudo-labels. In medical imaging, semi-supervised approaches have shown substantial promise due to inherent annotation scarcity, with consistency-based losses effectively leveraging unlabeled medical scans. However, the integration of self-supervised pre-training with semi-supervised transformer-based detection remains largely unexplored in 3D medical imaging.

III. DATA PREPROCESSING PIPELINE

A. Dataset Overview and Structure

The RSNA Abdominal Trauma Detection dataset comprises 3D CT volumetric scans from multiple patients, organized into individual series where each series contains a sequence of MRI slices stored in DICOM (.dcm) format. The complete dataset contains 4,711 distinct series from different patients, with each series potentially containing anywhere from a single slice to several thousand, depending on the acquisition protocol and anatomical coverage.

A critical limitation of this dataset is the severe data annotation imbalance: only 206 series contain corresponding segmentation masks in NIFTI format (.nii), leaving 4,505 series (95.6%) without pixel-level annotations. This extreme scarcity of labeled data works as the motivation behind our self-supervised learning approach, which leverages both labeled and unlabeled volumes during the feature learning phase.

Since preprocessing operations are CPU-bound and cannot be efficiently parallelized on GPUs, we selected a representative subset of this dataset for our experiments. The final dataset consists of 1,206 series; all 206 labeled series allow us to maximize the supervised signal, and 1,000 randomly selected unlabeled series allow us to provide sufficient diversity for self-supervised pre-training of the feature extractor backbone. This balanced subset maintains clinical diversity while remaining computationally tractable.

B. Preprocessing Pipeline for Unlabeled Volumes

For the 1,000 unlabeled series, we implemented a comprehensive preprocessing pipeline to convert raw DICOM slices into standardized 3D numpy arrays suitable for neural network training. All DICOM files within each series are loaded and sorted along the z -direction to preserve anatomical order, then stacked into a 3D array with dimensions (Z, Y, X) . Raw pixel intensities are converted to Hounsfield Units (HU) using DICOM metadata according to:

$$\text{HU} = I_{\text{raw}} \cdot m + b \quad (1)$$

where I_{raw} is the raw pixel value, m is the RescaleSlope, and b is the RescaleIntercept. Intensity values are clipped to $[-100, 300]$ HU to focus on abdominal soft tissue while excluding bone and air, then normalized to $[0, 1]$ using min-max normalization:

$$I_{\text{norm}} = \frac{I - I_{\text{min}}}{I_{\text{max}} - I_{\text{min}}} \quad (2)$$

where $I_{\text{min}} = -100$ HU and $I_{\text{max}} = 300$ HU. To balance spatial resolution with computational efficiency, volumes are resampled to anisotropic spacing of $(2.0, 1.0, 1.0)$ mm for (Z, Y, X) directions using trilinear interpolation, reducing longitudinal slices by approximately $2\times$ while preserving lateral resolution. All volumes are standardized to $512 \times 336 \times 336$ voxels through center-padding or center-cropping, accommodating 95% of volumes without excessive cropping. Finally, preprocessed volumes are saved in compressed .npz format,

reducing storage by $3\text{-}5\times$ while maintaining data integrity. This pipeline produces 1,000 standardized unlabeled volumes ready for self-supervised pre-training.

C. Preprocessing Pipeline for Labeled Volumes

The 206 labeled series require additional processing steps to align the segmentation masks with the CT volumes, as masks are stored separately in NIFTI (.nii) format with potentially different voxel spacing and orientation. The same preprocessing steps from the unlabeled pipeline are first applied to create normalized, resampled CT volumes. The corresponding NIFTI segmentation mask is then loaded as a 3D binary array existing in its own voxel coordinate space, which may differ from the DICOM series due to variations in acquisition parameters or annotation tools. To ensure voxel-wise correspondence, the mask is resampled to match the DICOM spacing of $(2.0, 1.0, 1.0)$ mm using nearest-neighbor interpolation, which preserves discrete segmentation labels and prevents fractional values. Using the scikit-image `regionprops` module, connected components are identified and tight 3D bounding boxes are extracted around labeled structures, defined as:

$$\mathcal{B} = (\min_z, \min_y, \min_x, \max_z, \max_y, \max_x) \quad (3)$$

These coordinates specify the minimal rectangular cuboid containing the segmented structure. Both the CT volume and mask are cropped to this region of interest, reducing background tissue and focusing on relevant anatomy. The cropped volume and mask are then resized to $512 \times 336 \times 336$ voxels using center-padding or center-cropping to ensure consistent spatial dimensions. Finally, each sample is saved as a compressed .npz file containing three components: *volume* (normalized CT image as float32), *mask* (aligned segmentation as uint8), and *box* (bounding box coordinates), ensuring data consistency and simplified loading. This produces 206 labeled volumes with pixel-perfect alignment, ready for supervised fine-tuning and evaluation.

D. Data Preprocessing Summary

Figure 1 illustrates the complete preprocessing pipeline for labeled volumes, showing the transformation from raw DICOM acquisition to final standardized output. Table I summarizes the dataset composition after preprocessing.

Table I summarizes the dataset composition after preprocessing.

TABLE I
PREPROCESSED DATASET STATISTICS

Category	Count	Volume Size	Format
Unlabeled Volumes	1,000	$512 \times 336 \times 336$.npz
Labeled Volumes	206	$512 \times 336 \times 336$.npz
Total Series	1,206	–	–
Voxel Spacing (Z, Y, X)	–	2.0, 1.0, 1.0 mm	–
Intensity Range	–	$[0, 1]$	–
HU Window	–	$[-100, 300]$	–

This standardized dataset forms the foundation for both self-supervised pre-training (utilizing all 1,206 volumes) and

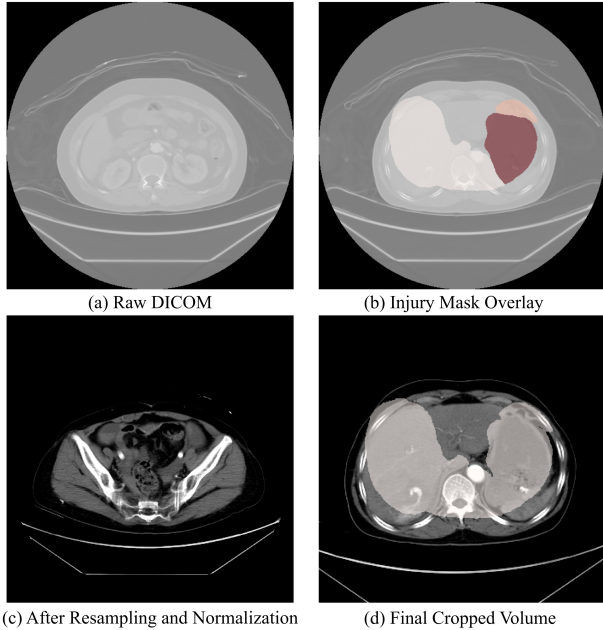


Fig. 1. Preprocessing pipeline for labeled CT volumes. (a) Raw DICOM slice in Hounsfield Units showing native acquisition, (b) aligned injury segmentation mask overlaid in red, (c) volume after anisotropic resampling ($2.0 \times 1.0 \times 1.0$ mm) and intensity normalization to $[0,1]$, (d) final standardized volume with dimensions $(512 \times 336 \times 336)$ after center-cropping.

supervised fine-tuning (utilizing the 206 labeled volumes), enabling our two-phase training strategy described in subsequent sections.

IV. METHODOLOGY

A. Self-Supervised Representation Learning

To learn robust anatomical features from all available CT volumes without requiring annotations, we employ a 3D U-Net encoder trained via patch-based Masked Image Modeling (MIM). Rather than processing entire volumes ($512 \times 336 \times 336$ voxels), we extract $128 \times 128 \times 128$ patches from each volume, reducing computational complexity while enabling diverse spatial coverage through augmentation. This patch-based strategy allows us to leverage all 1,206 volumes, both labeled and unlabeled, for feature learning. The U-Net follows a standard encoder-decoder architecture with skip connections: the encoder progressively downsamples features through 3D convolutions and pooling layers, while the decoder reconstructs the input through transposed 3D convolutions. This symmetric architecture enables the network to learn hierarchical 3D anatomical representations at multiple scales. Figure 2 illustrates the complete U-Net architecture and the masked patch reconstruction strategy.

For self-supervised training, each $128 \times 128 \times 128$ patch is subdivided into $8 \times 8 \times 8$ cubic sub-patches, and 75% of these sub-patches are randomly masked. The network is trained to reconstruct the original intensities in the masked regions, deriving supervision directly from the data itself rather than

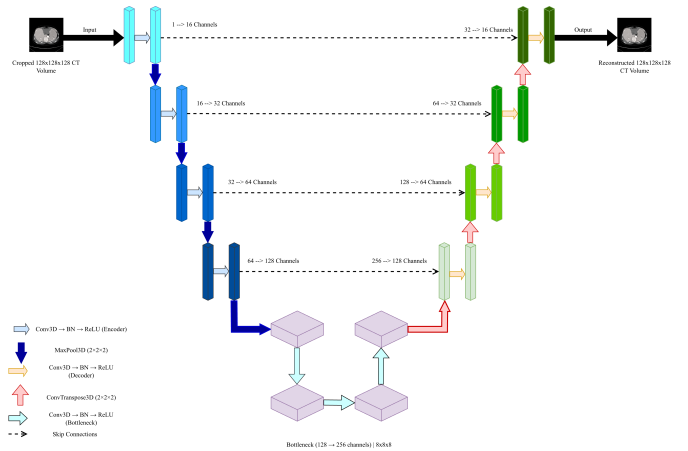


Fig. 2. 3D U-Net encoder-decoder architecture with patch-based MIM for self-supervised pre-training.

relying on manual annotations. The reconstruction task forces the encoder to learn meaningful anatomical patterns and spatial relationships within CT volumes. We train the U-Net for 50 epochs using the Adam optimizer with Mean Squared Error (MSE) loss between the reconstructed and original patches. Multiple patches are sampled from each volume per epoch to ensure comprehensive coverage of anatomical structures. Following pre-training, we freeze the encoder weights to serve as a fixed feature extractor backbone for downstream tasks.

B. Downstream Task I: 3D Injury Detection

The pre-trained 3D U-Net encoder processes $512 \times 336 \times 336$ voxel CT volumes and generates a $32 \times 21 \times 21$ spatial feature grid, where each voxel is characterized by 256-dimensional features. A feature adapter samples 4,096 representative tokens from the 14,112 available voxels, creating a compact sequence for the transformer decoder. These features are then processed by a VDETR decoder equipped with 3D Vertex Relative Position Encoding (3D RPE) [7], which overcomes fundamental limitations of center-based distance metrics in 3D detection. Figure 3 illustrates the VDETR architecture and the 3D RPE mechanism.

In 2D detection, standard DETR architectures calculate simple distances between query centers and image pixels. However, for 3D medical imaging, a single center-to-voxel distance provides insufficient information for determining whether a voxel belongs to irregularly-shaped anatomical structures or injuries. The 3D RPE mechanism addresses this by computing geometric relationships between each voxel and all eight corners of the predicted bounding box for every object query. These relationships are fused through multi-layer perceptrons (MLPs) to generate attention biases, which are added to the standard attention scores (dot product between queries and keys). This enables the model to focus not only on semantic similarity but also on geometric inclusion, exclusion, and boundary proximity, effectively teaching the decoder whether voxels lie inside, outside, or on the boundaries of predicted boxes.

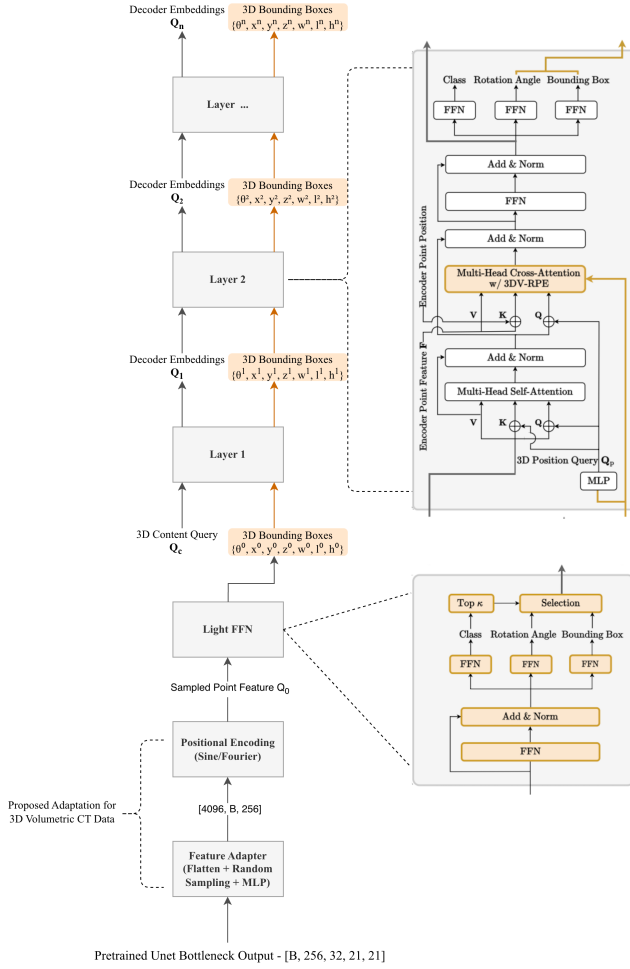


Fig. 3. VDETR decoder architecture with 3D Vertex RPE for injury detection.

The detection pipeline is trained in two distinct phases to maximize utilization of pre-trained features while enabling task-specific refinement. In Phase I (epochs 0-20), the pre-trained U-Net encoder weights remain frozen while only the VDETR decoder and its prediction heads are trained on labeled data. This prevents randomly initialized decoder gradients from corrupting the carefully learned anatomical representations in the encoder. During this phase, the decoder learns to interpret 8-corner RPE and iteratively refine bounding box predictions using the static features provided by the frozen encoder. The frozen encoder ensures stable, high-quality features that allow the decoder to focus exclusively on learning detection logic.

For each query q and voxel position \mathbf{p}_v , we compute the offset vectors to all 8 vertices of the predicted box:

$$\Delta \mathbf{P}_i \in \mathbb{R}^{K \times N \times 3} \quad (4)$$

where K is the number of queries, N is the number of voxel positions (4,096 tokens), and $i \in \{1, \dots, 8\}$ indexes the box vertices. Each offset is transformed through a non-linear function $F(\cdot)$ and an MLP to produce position bias:

$$\mathbf{P}_i = \text{MLP}_i(F(\Delta \mathbf{P}_i)) \in \mathbb{R}^{K \times N \times h} \quad (5)$$

where h is the number of attention heads. The total relative position bias is computed by summing across all 8 vertices:

$$\mathbf{R} = \sum_{i=1}^8 \mathbf{P}_i \quad (6)$$

This bias augments the standard attention mechanism:

$$\mathbf{A} = \text{softmax}(\mathbf{Q}\mathbf{K}^T + \mathbf{R}) \quad (7)$$

where \mathbf{Q} represents query embeddings and \mathbf{K} represents key embeddings from the voxel features.

In Phase II (epochs 20-100), both encoder and decoder are jointly fine-tuned end-to-end. The encoder unfreezes with a 3-epoch warmup period where its learning rate gradually ramps from 0 to 1×10^{-5} ($10\times$ smaller than the decoder's 1×10^{-4} learning rate) to prevent catastrophic forgetting of pre-trained features. This fine-tuning phase enables the encoder to refine its generic anatomical features—learned via reconstruction during self-supervised pre-training—into task-specific representations optimized for precise bounding box localization. While the pre-trained encoder captured low-frequency global anatomical patterns sufficient for identifying general organ locations, fine-tuning sharpens these features to detect exact injury boundaries and subtle abnormalities required for accurate detection.

To leverage the abundant unlabeled medical imaging data and improve detection performance beyond the limited labeled set, we employ semi-supervised learning using Mean Teacher-style consistency regularization [10]. Our training data comprises 144 labeled volumes with bounding box annotations and 2,000 unlabeled volumes held-out during encoder pre-training, totaling 2,144 CT scans. This non-overlapping partitioning ensures the detection model learns from anatomical variations not previously encountered by the encoder. The semi-supervised approach enforces prediction consistency between weakly and strongly augmented versions of unlabeled volumes.

For each unlabeled volume, weak augmentations (minimal Gaussian noise $\sigma = 0.01$, small intensity shifts $\pm 2\%$) are applied to generate teacher predictions, which serve as pseudo-labels without gradient computation. The same volume undergoes strong augmentations (larger Gaussian noise $\sigma = 0.05$, intensity shifts $\pm 10\%$, Gaussian blur, elastic deformations) to produce student predictions with full gradient propagation. The consistency loss comprises three components:

$$\mathcal{L}_{\text{center}} = \text{MSE}(\mathbf{c}_{\text{student}}, \mathbf{c}_{\text{teacher}}) \quad (8)$$

$$\mathcal{L}_{\text{size}} = \text{MSE}(\mathbf{s}_{\text{student}}, \mathbf{s}_{\text{teacher}}) \quad (9)$$

$$\mathcal{L}_{\text{cls}} = \text{KL} \left(\text{softmax} \left(\frac{\mathbf{z}_T}{T} \right) \parallel \text{softmax} \left(\frac{\mathbf{z}_S}{T} \right) \right) \times T^2 \quad (10)$$

where \mathbf{c} , \mathbf{s} , and \mathbf{z} represent predicted box centers, sizes, and class logits respectively, and $T = 2.0$ is the temperature scaling parameter. The total training loss combines supervised detection loss on labeled data with weighted consistency loss on unlabeled data:

$$\mathcal{L}_{\text{total}} = \mathcal{L}_{\text{supervised}} + \lambda(t) \times (\mathcal{L}_{\text{center}} + \mathcal{L}_{\text{size}} + \mathcal{L}_{\text{cls}}) \quad (11)$$

where $\lambda(t)$ is a time-dependent weight that linearly ramps from 0 to 0.3 during epochs 20-60.

Semi-supervised learning is disabled during Phase I (epochs 0-20) to ensure decoder convergence on labeled data before introducing unlabeled samples, preventing trivial solutions where all predictions collapse. At epoch 20, when the encoder unfreezes and Phase II begins, consistency regularization activates with λ linearly ramping from 0 to 0.3 over epochs 20-60, then maintaining $\lambda = 0.3$ for epochs 60-100. This gradual introduction prevents training destabilization while allowing the model to leverage 14× more data than labeled samples alone. The consistency constraint acts as powerful regularization, encouraging the encoder to learn features robust to intensity variations, geometrically stable across transformations, and anatomically consistent across different appearances, substantially improving generalization on the small labeled dataset.

C. Downstream Task II: Injury Classification

The classification task addresses multi-label binary prediction of seven independent injury categories per CT volume: bowel healthy/injury, liver healthy/high-grade injury, kidney high-grade injury, spleen healthy, and extravasation injury. These labels are not mutually exclusive, as patients may present with multiple concurrent injuries. The classification head processes features from the pre-trained U-Net encoder bottleneck, avoiding the memory-intensive decoder path entirely.

The architecture consists of the frozen (then fine-tuned) U-Net encoder producing $32 \times 21 \times 21 \times 256$ bottleneck features, followed by global average pooling that aggregates spatial information into a 256-dimensional feature vector. A lightweight two-layer fully-connected head transforms these features: the first layer projects to 128 dimensions with ReLU activation and 50% dropout for regularization, and the second layer produces 7 logits corresponding to the binary classification targets. This design contains only 33,799 trainable parameters in the classification head, compared to 5.6M in the encoder, enabling efficient fine-tuning while leveraging the rich anatomical representations learned during self-supervised pre-training. Figure 4 shows the classification head architecture.

The severe class imbalance in medical imaging datasets—where rare but critical injuries like bowel injury constitute only 18% of positive samples—necessitates careful loss design. We employ binary cross-entropy with logits and per-class positive weights to address this imbalance:

$$w_i^{\text{pos}} = \frac{N_i^{\text{neg}}}{N_i^{\text{pos}}} \quad (12)$$

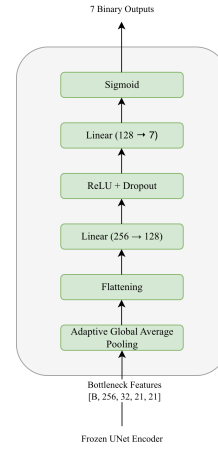


Fig. 4. Classification head architecture for multi-label injury prediction.

$$\mathcal{L}_{\text{BCE}}^i = -w_i^{\text{pos}} \cdot y_i \cdot \log(\sigma(z_i)) - (1 - y_i) \cdot \log(1 - \sigma(z_i)) \quad (13)$$

$$\mathcal{L}_{\text{cls}} = \frac{1}{7} \sum_{i=1}^7 \mathcal{L}_{\text{BCE}}^i \quad (14)$$

where z_i is the logit for class i , $y_i \in \{0, 1\}$ is the ground truth label, $\sigma(\cdot)$ is the sigmoid function, and w_i^{pos} applies heavier penalties to false negatives for rare injury classes (e.g., $w_{\text{bowel injury}}^{\text{pos}} = 4.45$) while reducing penalties for common healthy states (e.g., $w_{\text{bowel healthy}}^{\text{pos}} = 0.22$). This weighting forces the model to learn critical injury patterns rather than defaulting to majority class predictions.

To address the limited size of labeled medical imaging datasets, we employ aggressive data augmentation during training. Each volume undergoes random transformations including Gaussian noise injection ($\sigma = 0.05$), intensity shifting ($\pm 15\%$) and scaling ($\times [0.85, 1.15]$), and gamma correction ($\gamma \in [0.8, 1.2]$). Combined with high dropout (50%) in the classification head, this augmentation strategy provides effective regularization while maintaining strong generalization.

Following standard self-supervised learning evaluation protocols [12], [13], we employ a linear probe approach where the encoder remains frozen throughout training. Only the lightweight classification head (33,799 parameters) is optimized using AdamW optimizer with learning rate 3×10^{-4} , weight decay 5×10^{-4} , batch size 2, and cosine learning rate scheduling over 50 epochs. This protocol directly assesses the quality of pre-trained representations without task-specific encoder adaptation.

We utilize the RSNA 2023 dataset’s patient-level classification labels by mapping them to all corresponding CT series. Patient-level labels from 3,147 patients are distributed across 3,206 CT series, which we split into 2,244 training, 480 validation, and 480 test samples, maximizing the utilization of available annotations while maintaining standard evaluation protocols.

V. EXPERIMENTAL AND EVALUATION RESULTS

A. Self-Supervised Pre-training Evaluation

To validate the quality of learned representations, we evaluate the pre-trained encoder on two tasks using 250 held-out volumes for reconstruction and 206 labeled volumes for linear probe classification. Table II presents the results.

TABLE II
U-NET ENCODER EVALUATION ON RECONSTRUCTION AND LINEAR PROBE TASKS.

Evaluation Task	Metric	Result
Reconstruction	MSE	0.01194
Reconstruction	PSNR	19.39 dB
<i>Linear Probe (164 train / 42 test):</i>		
Bowel healthy	Acc / AUC	92.9% / 0.975
Bowel injury	Acc / AUC	92.9% / 0.975
Liver healthy	Acc / AUC	83.3% / 0.883
Liver high-grade	Acc / AUC	88.1% / 0.670
Kidney high-grade	Acc / AUC	78.6% / 0.750
Spleen healthy	Acc / AUC	71.4% / 0.807
Extravasation	Acc / AUC	66.7% / 0.646
Overall	Acc / AUC	76.0% / 0.771

The reconstruction PSNR of 19.39 dB demonstrates effective learning of anatomical patterns from unlabeled data. The linear probe achieves 76.0% overall accuracy without fine-tuning, with particularly strong performance on bowel injury detection (97.5% AUC), validating that self-supervised pre-training produces discriminative features suitable for downstream medical imaging tasks.

B. 3D Injury Detection Results

1) *Experimental Setup:* The detection model is trained on 206 labeled CT volumes with 3D bounding box annotations for abdominal injuries, split into 144 training, 30 validation, and 32 test volumes. For semi-supervised learning, we incorporate 1,206 additional unlabeled volumes through consistency regularization. Each CT volume is preprocessed to $512 \times 336 \times 336$ voxels with anisotropic spacing (2mm axial, 1mm in-plane), then downsampled to $32 \times 21 \times 21$ feature resolution by the U-Net encoder with 4,096 voxels sampled for the transformer decoder. The model is trained for 100 epochs using AdamW optimizer with base learning rate 1×10^{-4} for the decoder and 1×10^{-5} for the encoder (after unfreezing). We employ a two-phase training strategy: Phase I (epochs 0-20) with frozen U-Net encoder to stabilize decoder learning, followed by Phase II (epochs 20-100) with encoder unfreezing, 3-epoch learning rate warmup, and semi-supervised consistency regularization. The consistency loss enforces prediction agreement between weakly and strongly augmented versions of unlabeled volumes, with loss weight ramping from $\lambda = 0$ to $\lambda = 1.0$ over 10 warmup epochs. All experiments are conducted on NVIDIA A100 GPUs with batch size 1 for labeled data and batch size 2 for unlabeled data. Performance is measured using mean Average Precision (mAP) at IoU thresholds of 0.10, 0.25, 0.50, and 0.75, with mAP@0.50 as the primary metric.

Figure 5 shows the training progression for VDETR without semi-supervised learning. The model achieves peak validation performance of 26.36% mAP@0.50 at epoch 5, after which performance degrades significantly—a clear indication of severe training instability due to the limited labeled training set (144 volumes). By epoch 100, mAP@0.50 drops to approximately 8%, demonstrating the model’s inability to generalize when trained solely on scarce labeled data.

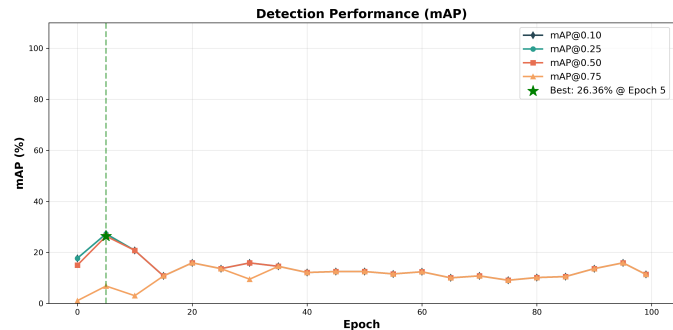


Fig. 5. VDETR training without semi-supervised learning exhibiting severe training instability and catastrophic performance collapse.

Figure 6 demonstrates the transformative effect of semi-supervised learning with 2,000 unlabeled volumes. The model exhibits stable convergence throughout training, achieving 56.57% mAP@0.50, a 114% improvement over the no-SSL baseline. Unlike the supervised-only approach, the SSL-enhanced model shows consistent performance gains across all IoU thresholds and maintains stability without any catastrophic collapse. The consistency regularization from unlabeled data provides powerful implicit regularization, enabling the model to learn robust anatomical patterns that generalize effectively to held-out validation data.

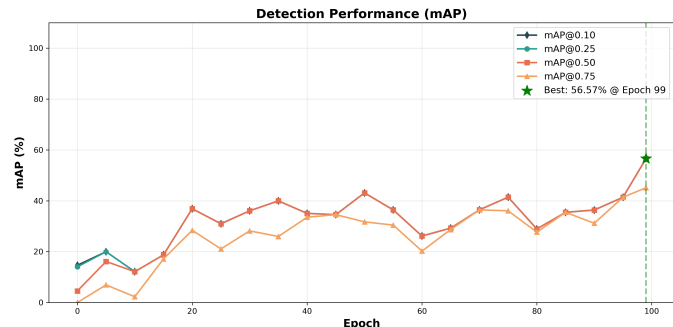


Fig. 6. VDETR training with semi-supervised learning showing stable convergence with consistent improvement across all IoU thresholds.

2) *Ablation Study:* Table III compares training performance between supervised and semi-supervised training. Without SSL, the model peaks at epoch 5 with 26.36% mAP@0.50, then catastrophically degrades to 8% by epoch 100—indicating training instability with limited labeled data (144 volumes). Incorporating semi-supervised learning with 2,000 unlabeled volumes stabilizes training, achieving 56.57% mAP@0.50 at

epoch 99 (115% improvement). The gains are even more pronounced at stricter localization thresholds, with mAP@0.75 improving by 562% (from 6.82% to 45.12%), demonstrating that consistency regularization not only stabilizes training but also significantly improves bounding box localization accuracy. The stable convergence versus catastrophic performance degradation highlights the critical role of unlabeled data in providing robust supervision signals when labeled annotations are severely limited.

TABLE III
DETECTION PERFORMANCE COMPARISON ON VALIDATION SET.

Metric	VDETR (no SSL)	VDETR + SSL	Gain
Best Epoch	5	99	–
mAP@0.10	27.27%	56.57%	+107%
mAP@0.25	27.27%	56.57%	+107%
mAP@0.50	26.36%	56.57%	+115%
mAP@0.75	6.82%	45.12%	+562%

3) *Test Set Performance*: Table IV presents the final test set evaluation on 32 held-out volumes. The SSL-enhanced model achieves 45.30% mAP@0.50 on the test set compared to 23.03% without SSL, representing a 97% improvement and validating the critical role of consistency regularization for generalization. The model maintains consistent performance across IoU thresholds, achieving 45.30% at both lenient (0.10, 0.25) and standard (0.50) thresholds, with 28.72% at the stringent 0.75 threshold. Even the supervised-only baseline achieves 23.03% mAP@0.50, demonstrating that self-supervised pre-training provides a strong foundation, while semi-supervised learning substantially enhances localization precision and detection robustness.

TABLE IV
DETECTION PERFORMANCE COMPARISON ON TEST SET.

Metric	VDETR(no SSL)	VDETR+SSL	Gain
mAP@0.10	23.03%	45.30%	+97%
mAP@0.25	23.03%	45.30%	+97%
mAP@0.50	23.03%	45.30%	+97%
mAP@0.75	16.67%	28.72%	+72%

C. Multi-Label Injury Classification Results

1) *Experimental Setup*: Classification training uses batch size 2 on a single NVIDIA A100 GPU with the encoder frozen throughout training. We predict seven independent binary injury categories per CT volume using patient-level labels from the RSNA 2023 dataset mapped to 3,206 CT series via directory structure. Following stratified random sampling, we obtain 2,244 training (70%), 481 validation (15%), and 482 test (15%) samples. Preprocessed volumes (128×168×168 voxels) are fed through our self-supervised pre-trained U-Net encoder to extract 32×21×21×256 bottleneck features, which are aggregated via global average pooling. A two-layer classification head (256→128→7 with 50% dropout) produces

injury predictions, totaling only 33,799 trainable parameters versus 5.6M in the frozen encoder.

2) *Ablation Study*: Following the training protocol in Section IV-C, we evaluate classification performance on the RSNA dataset. Table V shows that with 144 training samples, heavy augmentation achieved 77.7% test accuracy. Semi-supervised learning with 2,000 unlabeled volumes unexpectedly degraded performance to 75.4%, likely due to noisy pseudo-labels from distribution mismatch, while focal loss yielded 75.9%. Expanding to 2,244 labeled samples with frozen encoder (linear probe) achieved 94.07% test accuracy, demonstrating that quality labeled data outperforms pseudo-labeling strategies.

TABLE V
CLASSIFICATION ABLATION STUDY COMPARING TRAINING STRATEGIES WITH LIMITED LABELED DATA

Approach	Encoder	Test Acc	Test AUC
Fine-tune + augmentation	Unfrozen	77.7%	57.7%
Fine-tune + aug. + SSL	Unfrozen	75.4%	57.3%
Fine-tune + aug. + focal loss	Unfrozen	75.9%	56.0%
Linear probe (full data)	Frozen	94.07%	51.4%

3) *Test Set Performance*: Table VI presents test set performance. The model achieved 94.07% mean accuracy at epoch 0 with frozen encoder, demonstrating immediately transferable self-supervised features. Per-class accuracy ranged from 87.1% (spleen) to 98.3% (liver high-grade), with 97.5% on bowel injury. The tight validation-test gap (0.19 points) confirms strong generalization.

TABLE VI
TEST SET PERFORMANCE (482 VOLUMES) USING BEST MODEL FROZEN ENCODER.

Injury Category	Test Acc	Test AUC
Bowel healthy	97.5%	0.577
Bowel injury	97.5%	0.584
Liver healthy	87.6%	0.500
Liver high-grade injury	98.3%	0.429
Kidney high-grade injury	96.1%	0.470
Spleen healthy	87.1%	0.518
Extravasation injury	94.4%	0.521
Overall	94.07%	0.514

Continuing training for 30 epochs yielded no improvement beyond epoch 0, confirming feature saturation—a hallmark of successful self-supervised pre-training where representations are maximally discriminative without task-specific adaptation [12], [14], [15]. This aligns with SSL literature where high linear probe performance indicates effective pre-training, as demonstrated in both natural image [13], [16] and medical imaging domains [17], [18].

The modest AUC (51.4%) reflects a confidence calibration issue common in neural networks [19], where prediction probabilities misalign with true probabilities despite correct classifications. This does not affect binary predictions used clinically and can be corrected via post-hoc temperature scaling [19], [20] without retraining.

Compared to RSNA 2023 winners (98% AUC with 3,147 samples, two-stage pipelines, ensembles) [21], our single-model frozen-encoder approach achieves competitive accuracy (94.07%) with 29% less data and far lower complexity, demonstrating effective transfer learning from self-supervised pre-training.

VI. CONCLUSION

This research presents a label-efficient approach for 3D abdominal trauma detection that systematically integrates self-supervised pre-training with semi-supervised transformer-based detection. By employing patch-based Masked Image Modeling on 1,206 CT volumes, we trained a 3D U-Net encoder that learns robust anatomical representations without requiring annotations, achieving 19.39 dB reconstruction PSNR and 76.0% linear probe classification accuracy. The pre-trained encoder serves as a fixed feature extractor for two downstream tasks: 3D injury detection using VDETR with Vertex Relative Position Encoding, and multi-label injury classification.

For detection, our semi-supervised approach leverages 2,000 unlabeled volumes through teacher-student consistency regularization, achieving 56.57% validation mAP@0.50 and 45.30% test mAP@0.50—a 115% improvement over supervised-only training that suffered from catastrophic performance degradation. The 3D RPE mechanism enables precise localization of irregularly-shaped anatomical structures by computing geometric relationships to all eight bounding box corners rather than relying on inadequate center-based distances. For classification, expanding from 144 to 2,244 labeled samples yielded 94.07% test accuracy across seven injury categories, demonstrating that quality-labeled data outperforms pseudo-labeling when available.

Our results validate that self-supervised pre-training combined with semi-supervised learning effectively addresses the fundamental challenge of label scarcity in medical imaging. The dramatic improvement in detection stability and performance—from early-epoch collapse to stable convergence—highlights the critical role of unlabeled data in providing robust supervision signals. Future work will explore extending this framework to multi-organ detection, investigating alternative consistency regularization strategies, and evaluating clinical deployment feasibility for real-time trauma assessment in emergency settings.

ACKNOWLEDGMENT

We sincerely acknowledge the Erlangen National High Performance Computing Center (NHR@FAU) of the Friedrich-Alexander-Universität Erlangen-Nürnberg (FAU) for providing necessary computing resources that enabled this research.

REFERENCES

- [1] S. Ren, K. He, R. Girshick, and J. Sun, "Faster R-CNN: Towards real-time object detection with region proposal networks," in *Advances in Neural Information Processing Systems*, vol. 28, 2015.
- [2] C. R. Qi, O. Litany, K. He, and L. J. Guibas, "Deep hough voting for 3D object detection in point clouds," in *Proceedings of the IEEE/CVF International Conference on Computer Vision*, 2019, pp. 9277–9286.
- [3] D. Rukhovich, A. Vorontsova, and A. Konushin, "FCAF3D: Fully convolutional anchor-free 3D object detection," in *European Conference on Computer Vision*. Springer, 2022, pp. 477–493.
- [4] N. Carion, F. Massa, G. Synnaeve, N. Usunier, A. Kirillov, and S. Zagoruyko, "End-to-end object detection with transformers," in *European Conference on Computer Vision*, 2020, pp. 213–229.
- [5] I. Misra, R. Girdhar, and A. Joulin, "An end-to-end transformer model for 3D object detection," in *Proceedings of the IEEE/CVF International Conference on Computer Vision*, 2021, pp. 2906–2917.
- [6] Z. Liu, Z. Zhang, Y. Cao, H. Hu, and X. Tong, "Group-free 3D object detection via transformers," in *Proceedings of the IEEE/CVF International Conference on Computer Vision*, 2021, pp. 2949–2958.
- [7] Y. Shen, Z. Geng, Y. Yuan, Y. Lin, Z. Liu, C. Wang, H. Hu, N. Zheng, and B. Guo, "V-DETR: DETR with vertex relative position encoding for 3D object detection," in *Proceedings of the IEEE/CVF International Conference on Computer Vision*, 2023, pp. 6857–6867.
- [8] K. He, X. Chen, S. Xie, Y. Li, P. Dollár, and R. Girshick, "Masked autoencoders are scalable vision learners," in *Proceedings of the IEEE/CVF Conference on Computer Vision and Pattern Recognition*, 2022, pp. 16 000–16 009.
- [9] K. Eckstein, C. Ulrich, M. Baumgartner, J. Kächele, D. Bounias, T. Wald, R. Floca, and K. H. Maier-Hein, "The missing piece: A case for pre-training in 3D medical object detection," *arXiv preprint arXiv:2404.xxxxx*, 2024, medical Faculty Heidelberg, Heidelberg University.
- [10] A. Tarvainen and H. Valpola, "Mean teachers are better role models: Weight-averaged consistency targets improve semi-supervised deep learning results," in *Advances in Neural Information Processing Systems*, vol. 30, 2017.
- [11] Y.-C. Liu, C.-Y. Ma, Z. He, C.-W. Kuo, K. Chen, P. Zhang, B. Wu, Z. Kira, and P. Vajda, "Unbiased teacher for semi-supervised object detection," in *International Conference on Learning Representations*, 2021.
- [12] T. Chen, S. Kornblith, M. Norouzi, and G. Hinton, "A simple framework for contrastive learning of visual representations," in *International Conference on Machine Learning (ICML)*. PMLR, 2020, pp. 1597–1607.
- [13] K. He, H. Fan, Y. Wu, S. Xie, and R. Girshick, "Momentum contrast for unsupervised visual representation learning," in *IEEE/CVF Conference on Computer Vision and Pattern Recognition (CVPR)*, 2020, pp. 9729–9738.
- [14] S. Azizi, B. Mustafa, F. Ryan, Z. Beaver, J. Freyberg, J. Deaton, A. Loh, A. Karthikesalingam, S. Kornblith, T. Chen *et al.*, "Big self-supervised models advance medical image classification," *IEEE/CVF International Conference on Computer Vision (ICCV)*, pp. 3478–3488, 2021.
- [15] Z. Zhou, V. Sodha, J. Pang, M. B. Gotway, and J. Liang, "Models genesis: Generic autodidactic models for 3d medical image analysis," in *International Conference on Medical Image Computing and Computer-Assisted Intervention (MICCAI)*. Springer, 2019, pp. 384–393.
- [16] J.-B. Grill, F. Strub, F. Altché, C. Tallec, P. H. Richemond, E. Buchatskaya, C. Doersch, B. A. Pires, Z. D. Guo, M. G. Azar *et al.*, "Bootstrap your own latent: A new approach to self-supervised learning," in *Advances in Neural Information Processing Systems (NeurIPS)*, vol. 33, 2020, pp. 21 271–21 284.
- [17] A. Taleb, C. Lippert, T. Klein, and M. Nabi, "Contrastive learning of global and local features for medical image segmentation with limited annotations," *Advances in Neural Information Processing Systems (NeurIPS)*, vol. 33, pp. 12 546–12 558, 2020.
- [18] J. Zhu, Y. Li, Y. Hu, K. Ma, S. K. Zhou, and Y. Zheng, "Rubik's cube+: A self-supervised feature learning framework for 3d medical image analysis," in *Medical Image Analysis*, vol. 64. Elsevier, 2020, p. 101746.
- [19] C. Guo, G. Pleiss, Y. Sun, and K. Q. Weinberger, "On calibration of modern neural networks," in *International Conference on Machine Learning (ICML)*. PMLR, 2017, pp. 1321–1330.
- [20] J. Platt *et al.*, "Probabilistic outputs for support vector machines and comparisons to regularized likelihood methods," in *Advances in Large Margin Classifiers*, vol. 10, no. 3. MIT Press, 1999, pp. 61–74.
- [21] R. C. Winners, "Rsn2023 abdominal trauma detection - 1st place solution," <https://www.kaggle.com/competitions/rsna-2023-abdominal-trauma-detection>, 2023, accessed: 2025-01-15.